Performance Losses and Current-Driven Recovery from Cation Contaminants in PEM Water Electrolysis

Journal of The Electrochemical Society, 2024 **171** 064510

Performance Losses and Current-Driven Recovery from Cation Contaminants in PEM Water Electrolysis

Elliot Padgett,[1,z] Anthony Adesso,[1] Haoran Yu,[2] Jacob Wrubel,[1] Guido Bender,[1] Bryan Pivovar,[1] and Shaun M. Alia[1]

[1]*Chemistry and Nanoscience Center, National Renewable Energy Laboratory, Golden, Colorado, United States of America*
[2]*Center for Nanophase Materials Sciences, Oak Ridge National Laboratory, Oak Ridge, Tennessee, United States of America*

Water contaminants are a common cause of failure for polymer electrolyte membrane (PEM) electrolyzers in the field as well as a confounding factor in research on cell performance and durability. In this study, we investigated the performance impacts of feed water containing representative tap water cations at concentrations ranging from 0.5–500 μM, with conductivities spanning from ASTM Type II to tap-water levels. We present multiple diagnostic signatures to help identify the presence of contaminants in PEM electrolysis cells. Through analysis of polarization curves and impedance spectroscopy to understand the origins of performance losses, we found that a switch from the acidic to alkaline hydrogen evolution mechanism is a key factor in contaminated cell behavior. Finally, we demonstrated that this mechanism switching can be harnessed to remove cation contaminants and recover cell performance without the use of an acid wash. We demonstrated near-complete recovery of cells contaminated with sodium and calcium, and partial recovery of a cell contaminated with iron, which was further investigated by post-mortem microscopy. The improved understanding of contaminant impacts from this work can inform development of strategies to mitigate or recover performance losses as well as improve the consistency and rigor of electrolysis research.
 [DOI: 10.1149/1945-7111/ad576b]

Manuscript submitted April 16, 2024; revised manuscript received May 31, 2024. Published June 27, 2024.

Supplementary material for this article is available online

Polymer electrolyte membrane water electrolysis (PEMWE) is a key technology for the clean energy transition, enabling clean and renewable energy to be utilized for hard-to-decarbonize applications in industry and transportation.[1,2] To achieve widespread production of clean hydrogen at ambitious cost targets such as the US Department of Energy's goal of $\$1/kg_{H2}$,[3] it is essential to optimize the efficiency, durability, and reliability of PEMWE. Water quality is an important factor impacting these aspects of PEMWE. High purity water is widely recognized as required at minimum to be ASTM Type II (>1 MΩ cm) or preferably ASTM Type I (>10 MΩ cm).[4–7]

However, several aspects of water quality warrant more careful investigation. For one, water contamination is a very common cause of failure, accounting for >80% of PEM electrolyzer failures in the field.[8–10] Dilute contaminants, below levels that cause short-term failure, can also harm operating efficiency and lead to more rapid degradation.[11–13] Furthermore, inconsistent water quality and contaminants also commonly impact PEM electrolysis devices in a research setting,[14,15] confusing measurements of cell performance and durability if they are not recognized and properly addressed. While water purification is a relatively minor direct contribution to PEMWE hydrogen production costs,[16,17] inadequate management of contaminants ultimately increases costs by harming efficiency, durability, and reliability, impacting the overall viability of PEMWE.

Considering the prevalence of contamination-related problems in PEMWE, a relatively small body of literature has systematically investigated contaminants in PEMWE cells specifically.[4,11,18–25] The published literature suggests that cation contaminants are the most common class of contaminants causing significant performance impacts in PEMWE, especially by displacement of protons in the membrane. Some metals (such as Cu) can also poison the cathode catalyst by electrochemical deposition on the Pt surface,[23] but this is a less general phenomenon. The possible impacts of organic contaminants and anions are relatively unknown.[4] Cation contaminants in PEMWE can be grouped into two broad categories by source: 1) "exogenous" contaminants that result from inadequate purification of the water source, especially cations that are abundant in tap and ground water (Na^+, Ca^{2+}, Mg^{2+}, K^+, etc.) and 2) "endogenous" contaminants that originate from cell or system components, especially metals such as Fe, Cr, and Ni.[4] Several studies have incidentally identified cations contaminants as contributing to degradation. Wei et al.[13] and Sun et al.[12] both found accumulation of contaminants in recirculated water to be a primary cause of long-term performance decay and demonstrated recovery from acid washing of membrane electrode assemblies (MEAs). Rakouski[26] reported Ti contamination from an uncoated Ti porous transport layer (PTL) present in anode and cathode catalyst layers.

Further investigation to advance scientific understanding of contaminant impacts in PEMWE offers the opportunity to develop improved strategies for mitigation of contaminant impacts and recovery of contaminated cells. Contaminants are currently mitigated at the system level through water purification subsystems and conductivity sensors.[17] To our knowledge, no specific cell-level mitigation strategies have been reported, and it is difficult to conceive of how this would be effectively accomplished. Existing reported recovery procedures include washing with sulfuric acid, either by disassembly of the cell and soaking the MEA[12,13] or by flowing acid through the cell,[20,24] although this strategy presents challenges for implementation at stack scale and in the field. Babic et al.[21] reported an alternative strategy using pressurized CO_2 to generate carbonic acid in situ for contaminant removal.

Efforts to understand contaminant impacts in PEMWE can leverage the more extensive literature focused on contaminant impacts in PEM fuel cells.[4,27–31] The basic phenomena of cation contamination in PEM fuel cells are well understood. Contaminant cations displace protons in the polymer electrolyte membrane, which harms protonic conductivity. Furthermore, the electric field that drives current in the membrane causes cations to concentrate in the cathode, leading to kinetic and thermodynamic performance impacts as well. With sufficiently large numbers of contaminant cations and a strong enough field, protons can be almost entirely depleted in the cathode, leading to a limiting current behavior.

Consistent with expectations from PEM fuel cells, Zhang et al.[18,19] used a reference electrode to demonstrate that sodium contaminants in PEMWE primarily impact the cathode potential and showed that the cell voltage impact grows abruptly at high current densities. Babic et al.,[21] Zlobinski et al.,[22] and Schalenbach et al.[24] also demonstrated cation accumulation in the cathode using neutron

[z]E-mail: elliot.padgett@nrel.gov

imaging and numerical modelling. However, some important differences have been demonstrated for cation contaminants in PEMWE vs PEM fuel cells as well. Notably, Zhang et al.[18,19] demonstrated that when Na^+ contaminants are introduced through the anode feed water, the pH of the water increases at the cathode outlet, implying that a significant number of contaminant cations can also leave the cell at the cathode. These investigations also showed that some cell performance is recovered simply by returning to clean DI water, without any acid wash or other deliberate recovery procedure. Together, these findings imply that cation contaminants can dynamically enter and leave the PEMWE cell, although the mechanisms and rates of these processes are not well understood. Zhang et al.[18,19] and Schalenbach et al.[24] have proposed that severe depletion of protons in the cathode will cause the hydrogen evolution reaction (HER) mechanism to change from the acidic to alkaline form. This can allow contaminant cations to associate with hydroxide anions generated in the alkaline HER, enabling a potential mechanism of escape from the polymer electrolyte. Understanding the mechanisms available for cation removal presents an important opportunity to develop new strategies for contaminant performance loss mitigation.

Here we will present first an investigation into the performance impacts of cation contaminants and second an investigation of recovery through a current-driven process. The investigation of performance impacts focuses on cation contaminants that are abundant in tap or ground water, with Na^+, K^+, and Ca^{2+} selected as representative ions. We report the performance impacts for cation concentrations ranging from tap-water-like to dilute ASTM Type II solutions, with impedance spectroscopy used to inform the origin of performance losses. We also present multiple diagnostic signatures to help identify the presence of contaminants in PEM electrolysis cells. This investigation provides evidence that a switch from acidic to alkaline HER plays a key role in performance impacts, as well as providing a route to enable cation removal. We further investigate the recovery of cells with different contaminants, including Na^+ and Ca^{2+}, as well as Fe^{3+} (as a representative transition metals and trivalent ions) that may leach out of PEMWE system components. We demonstrate that a current-driven recovery process provides almost complete recovery of performance impacts from Na^+ and Ca^{2+} contaminants, but only partial recovery from Fe^{3+}.

Methods

Cell materials and fabrication.—Catalyst coated membranes (CCMs) were fabricated by ultrasonic spray coating directly onto Nafion™ N115, with the cathode catalyst layer coated before the anode catalyst layer. The cathode catalyst layer contained Pt on high surface area carbon (Pt/HSC, Tanaka Kikinzoku Kogyo, TEC10E50E) with a targeted ionomer (Nafion™ D2020) to carbon ratio of 0.45:1. The ink for cathode spray coating was prepared at a concentration of 1 mg_{Pt}/mL in a solution of DI water and n-propyl alcohol (nPA) at a ratio of 1:0.95 (water:nPA), pre-chilled with ice, and mixed for 30 s in a probe ultrasonicator, followed by 15 min in an ice-water-filled bath ultrasonicator. Anode catalyst layers contained unsupported Ir oxide (Alfa Aesar) with an ionomer (Nafion™ D2020) to catalyst ratio of 0.2:1. The ink for anode spray coating was prepared at a concentration of 2.75 mg_{Ir}/mL in a solution of DI water and n-propyl alcohol (nPA) at a ratio of 1:0.95 (water:nPA), pre-chilled with ice, and mixed for 2 min in a probe ultrasonicator, followed by 30 min in an ice-water-filled bath ultrasonicator. Catalyst loadings were measured by XRF (Fischer XDV-SDD). For all CCMs, the cathode and anode catalyst loadings were 0.14 ± 0.01 mg_{Pt}/cm^2 and 0.40 ± 0.01 mg_{Ir}/cm^2, respectively. Assembled cells used a carbon paper cathode gas diffusion layer (AvCarb MGL280) at approximately 20% compression, set by PTFE gaskets, and a Pt-coated titanium felt anode PTL (Bekaert 2GDL10N).

General cell testing procedures.—Electrolyzer cell tests were conducted using an in-house constructed electrolyzer test station and custom hardware. The test hardware accommodates 25 cm^2 triple-serpentine, Pt/Au-coated (anode/cathode) titanium flow fields. For all cells used in this study the available flow-field area was masked down to create a 5 cm^2 active area. All cells were operated in a dry-cathode condition with an anode water flow rate of 50 ml min^{-1} supplied in a single-pass configuration. The inlet water temperature was controlled at 80 °C with a thermocouple at the anode inlet and the cell temperature was also regulated by heater pads placed on the hardware end plates, which were controlled by a thermocouple inserted into the anode flow field. Before performance testing, all cells were conditioned by stepping the cell voltage up to 1.85 V, holding this voltage for 10 h, and then recording 11 subsequent current-controlled polarization curves from 0.01–4 A cm^{-2}, for a total conditioning time of approximately 40 h. Conditioning and the high current recovery protocol used electrical power from the test station load bank, while performance, impedance, and cyclic voltammetry (CV) data reported in the paper were all recorded using an Autolab potentiostat/galvanostat with a 20 A booster (PGSTAT302N, Metrohm). Polarization curves covered a current density range from 10 mA cm^{-2} to 4 A cm^{-2} with approximately logarithmic spacing of the current density points and included both anodic and cathodic sweeps. Impedance spectra were recorded at each current density point, and each polarization curve required approximately 2.5 h with a total hold time of 4 min per point. The AC amplitude for impedance measurements was maintained in the range of 1%–5% of the DC current. High frequency resistance (HFR) values were calculated by interpolation of the Nyquist curve to find the real axis intercept. During CV measurements, the cathode side of the cell was supplied with humidified hydrogen at 100 sccm.

Contaminated feed water procedures.—Contaminants were introduced into the single-pass anode water feed using a syringe pump, as depicted in the schematic in Fig. 1a. The syringe pump injected a concentrated contaminant solution from a 60 ml syringe at a rate of 0.125 ml min^{-1} into the 50 ml min^{-1} DI water stream immediately before the anode inlet. The concentration of the syringe solution was adjusted to achieve the targeted feed water concentration. To minimize the delay time between starting the syringe pump and the introduction of contaminants to the cell, a valve was included at the connection between the concentrated solution line and the clean water feed to allow pre-filling of the concentrated solution line, with excess solution collected as waste. This configuration allows a constant controlled feed water composition while avoiding contaminating any parts of the test stand that are difficult to replace and could expose future experiments to contamination.

The typical procedure for measuring contaminant impacts is shown in Fig. 1b. For each experiment, an initial polarization curve was taken with clean DI water followed by a CV measurement. Afterwards, the cell was stepped up to a current density of 2 A cm^{-2}, and the contaminant solution was introduced after approximately 10 min. The current hold was then held for up to 3 h to observe cell voltage increases due to a dynamic response of the cell to contamination. For some cases with higher concentrations of contaminants the cell voltage reached a plateau, indicating the contamination process reached equilibrium, and the current hold was ended sooner than 3 h. Similar responses have been observed in fuel cells and methods have been developed to reproducibly quantify the contamination effect during the experiment.[32] In this work another polarization curve was taken with the contaminant solution still flowing through the cell to measure the effect of the contaminant across a range of current densities, followed by a final CV measurement.

The different contaminant salts and concentrations used are summarized in Table I. NaCl, KCl, and $CaCl_2$ contaminant salts were used at concentrations ranging from 0.5 to 500 μM. For each contaminant salt, a single cell was used for all different concentrations from low to high. Clean DI water flowed through the anode overnight between different concentrations of the same salt.

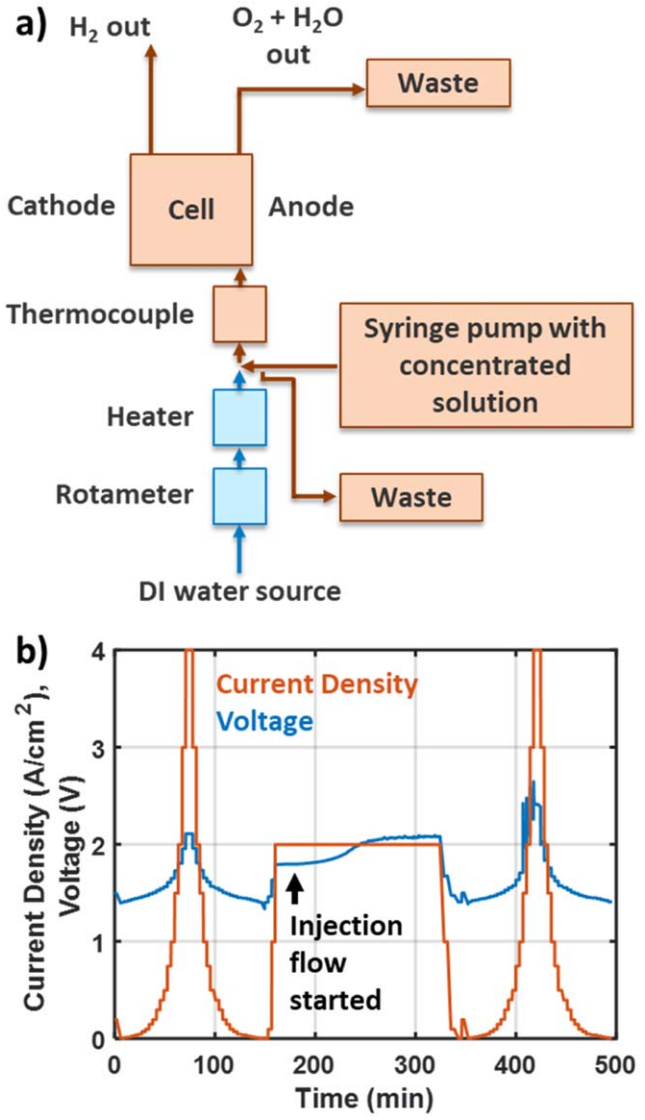

Figure 1. (a) Schematic of testing setup for contaminated water feeds for PEMWE cells. A concentrated solution of contaminants is injected into a single-pass DI water feed immediately before the cell anode inlet. Components and flow tubes that are exposed to contaminants are colored in red, while components that remain clean are colored in blue. Water lines were insulated between the heater and the cell, and contaminant injection before the thermocouple ensures that the water temperature at the cell inlet is controlled. (b) Plot of typical current and voltage profile for experiments measuring performance impacts from contaminated feed water. An initial polarization curve is recorded with clean water, then a 2 A cm^{-2} current hold is initiated during which the flow of contaminants is started. A final polarization curve is recorded with contaminated water flowing. Impedance spectra are recorded throughout the procedure at approximately 5 min intervals.

Between experiments with different salts, the exposed test station plumbing was disassembled and cleaned in DI water. Metal fittings and valves were sonicated in a large beaker of DI water for 30 min and periodically stirred. This process was repeated once with fresh DI water before drying the parts and reassembling the station. All plastic tubing was replaced with new tubing. Cell components including the CCM, GDL, PTL, and gaskets were replaced. The flow-fields were thoroughly rinsed with DI water and dried before reassembly of the cell.

Recovery protocols.—For the contaminant recovery experiments, a new cell was prepared and conditioned for each contaminant and beginning of life performance and impedance were measured. Contaminants were introduced to the cell at a 500 μM concentration in the anode water feed as the current was held at 2 A cm^{-2}. Contaminants were maintained in the feed water until a steady state voltage was achieved. For the first recovery protocol, "water rinse," the cell was left unpowered in an open circuit condition with clean DI water flowing over both the anode and cathode overnight (approximately 16 h), then a single polarization curve with impedance was recorded the next day. The cell was then re-contaminated following the same procedure described above, prior to the "polarization curve" recovery protocol. For this protocol, clean DI water was restored to the anode and seven consecutive polarization curves with impedance were recorded over approximately 18 h. The final "high current" recovery protocol was applied after this, without re-contaminating the cell, using the test station power supply rather than the potentiostat with booster to allow higher current densities. This protocol had several steps, as illustrated in Fig. S9, alternating between polarization curves and current holds. Each current hold section held at 2 A cm^{-2}, a higher current density, and then 2 A cm^{-2} again for 1 h each. The higher current densities were 4, 6, and 8 A cm^{-2}. This protocol was not designed to be optimal for contaminant removal in any way, but instead to incrementally increase the current applied to the cell while returning to a moderate reference current in between, providing opportunities to assess recovery. After this protocol was applied, a final polarization curve with impedance was recorded using the potentiostat and booster.

Microscopic characterization.—For cross-sectional analysis of MEAs using scanning transmission electron microscopy (STEM), small portions of MEA were embedded in epoxy and then cut by diamond-knife ultramicrotomy targeting a specimen thickness of ~75 nm. High-angle annular dark field scanning transmission electron microscopy (HAADF-STEM) and energy-dispersive X-ray spectrum (EDS) images were recorded using a JEM-ARM200F "NEOARM" analytical electron microscope (JEOL Ltd.) operated at 200 kV. The surface morphology and chemical composition of PTLs were examined using TESCAN MIRA3 GMH scanning electron microscope (SEM) operated at 20 kV.

Results and Analysis

Performance impacts of cation contaminants.—In this section we report on the performance impacts resulting from NaCl, KCl, and $CaCl_2$ contaminants in the anode feed water at a variety of different concentrations, as summarized in Table I. Cation concentrations were selected to span a range from tap-water-like[34] 500 μM solutions to dilute 0.5 μM solutions that qualify as ASTM Type II, as summarized in Table I along with conductivity/resistivity values. All experiments reported in this section followed the procedure illustrated in Fig. 1b: for each contaminant and concentration an initial polarization curve was recorded with clean water flowing to the anode, then a 2 A cm^{-2} current hold was initiated during which the flow of contaminants was started. A final polarization curve was then recorded with contaminated water.

Figure 2 shows the voltage response of cells exposed to the different contaminant solutions during the 2 A cm^{-2} current hold. Figure 2a compares the voltage impacts of different concentrations for each contaminant, shown on the same scale, while Fig. 2b compares the different contaminants at each concentration, with the scale narrowed to clearly show the trends at lower concentrations.

At 0.5 μM concentration (all ASTM Type II with 5.2–8.5 MΩ cm), none of the contaminants caused significantly accelerated voltage increases in comparison to a clean cell during the ~3 hr timeframe of these experiments. Note that the initial voltage observed for the different cells before contamination varies by approximately 10 mV due to minor performance variations between different cell assemblies. However, this voltage difference remains consistent after the introduction of contaminants, indicating that the voltage impact of the contaminants was negligible for this

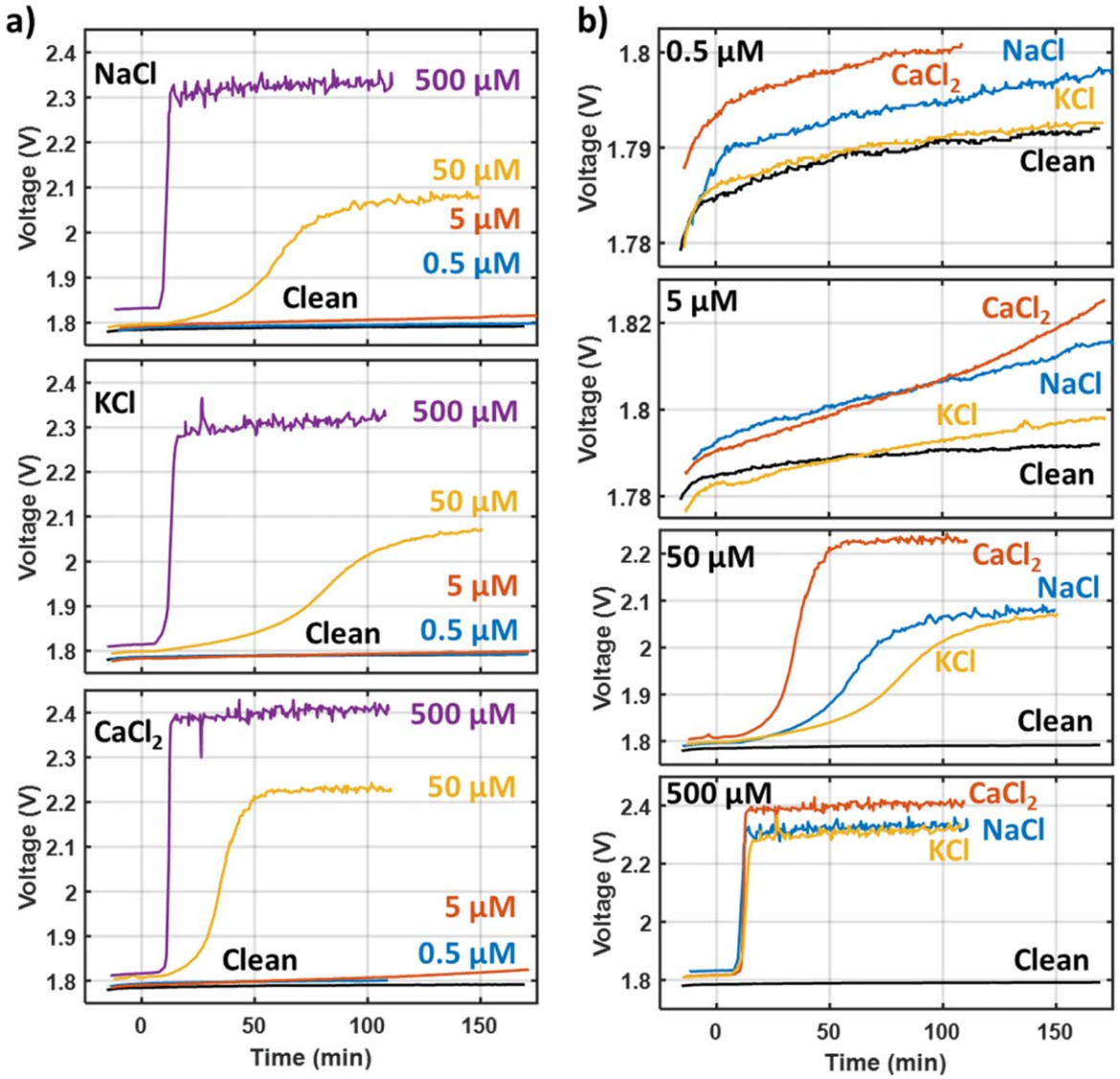

Figure 2. Cell voltage recorded over time at 2 A cm^{-2} as different contaminant salts are introduced at different concentrations from 0.5 μM to 500 μM, in comparison to the voltage response of a cell with clean feed water. A comparison between different concentrations of each contaminant is shown in (a) while a comparison between different contaminants at each concentration is shown in (b) using the same data. The contaminant syringe pump flow was started at approximately 0 min, although some delay (5–10 min) occurs before contaminants reach the cell.

Table I. Summary of contaminant solutions tested. Concentrations represent the overall diluted feed water concentration, rather than the concentrated solution supplied by the syringe pump. Water conductivity/resistivity is calculated using ionic conductivity values from the CRC Handbook of Chemistry and Physics.[33]

Contaminant salt	Cation concentration (μM)	Cation concentration (ppm or mg/L)	Water conductivity at 25 °C (μS/cm)	Water resistivity at 25 °C (MΩ cm)	Type[7]
None	0	0	0.055	18.3	ASTM Type I
NaCl	0.5	0.0115	0.12	8.5	ASTM Type II
	5	0.115	0.69	1.5	ASTM Type II
	50	1.15	6.4	0.16	Intermediate
	500	11.5	63	0.016	Tap-water-like
KCl	0.5	0.0195	0.13	7.7	ASTM Type II
	5	0.195	0.80	1.2	ASTM Type II
	50	1.95	7.6	0.13	Intermediate
	500	19.5	75	0.013	Tap-water-like
$CaCl_2$	0.5	0.02	0.19	5.2	ASTM Type II
	5	0.2	1.4	0.7	Intermediate
	50	2	13.6	0.07	Intermediate
	500	20	136	0.007	Tap-water-like
$FeCl_3$	500	28	217	0.005	—

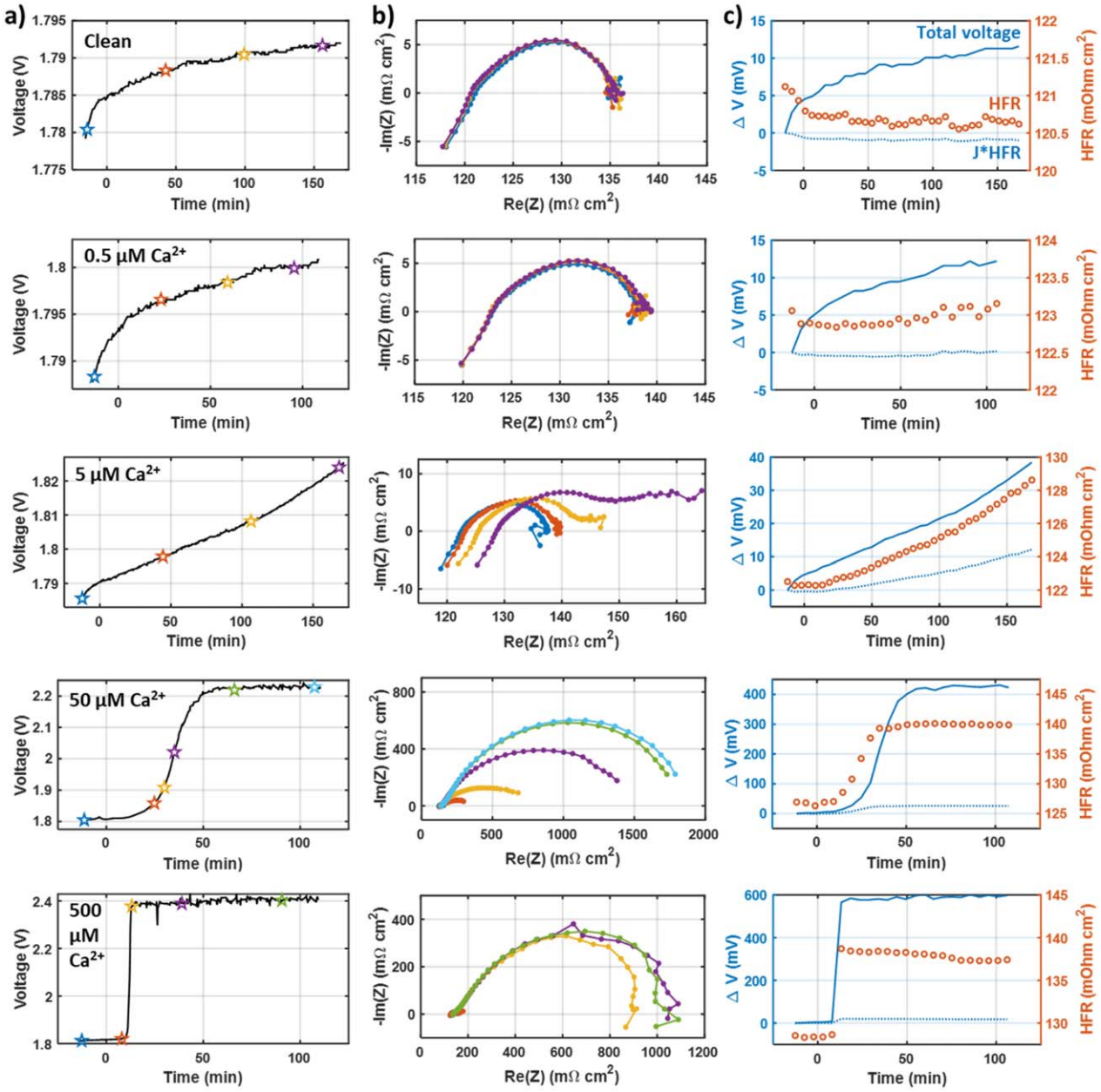

Figure 3. Investigation of the change in impedance occuring during contaminant introduction during 2 A cm^{-2} current holds. Voltage change over time (a) during the introduction of different contaminant solutions, with stars indicating time at which impedance curves (b) were sampled, with colors indicating corresponding curves and points. (c) Change in HFR, total voltage (solid line), and ohmic voltage (dotted line) resulting from HFR.

concentration and length of experiment. Over a longer time, such as tens or hundreds of hours, accumulation of contaminants in the cell may still lead to significant impacts. At 5 μM concentration (0.7–-1.5 MΩ cm, with NaCl and KCl solutions qualifying as ASTM Type II), all the contaminants resulted in significant additional voltage in comparison to a clean cell. This additional voltage appeared as a gradual voltage decay, although with a clearly increased rate. It is notable that even solutions meeting the ASTM Type II standard (>1 MΩ cm) can cause significant voltage impacts in short-term experiments.

Dramatically larger voltage losses were present for the 50 μM solutions (0.07–0.16 MΩ cm), which approached a voltage plateau within around 1–2 h. $CaCl_2$ caused a more severe voltage increase (over 400 mV) more rapidly in comparison to the NaCl and KCl (~300 mV), which is expected from the high selectivity for Ca^{2+} in Nafion™ as a divalent cation.[35,36] KCl was somewhat slower to impact the cell than NaCl, despite a higher ion exchange selectivity for K^+ in Nafion™ than Na^+,[36,37] likely because of the lower mobility of K^+ ions.[38] However, the final voltage loss for KCl was nearly identical to that for NaCl. At 500 μM concentration (0.007–0.016 MΩ cm, tap-water-like), all the contaminant solutions lead to dramatic voltage increases that plateaued rapidly, within minutes of their introduction to the cell. $CaCl_2$ resulted in a larger voltage increase (~600 mV) in comparison to NaCl and KCl (~500 mV), although the difference was not as dramatic as observed for the 50 μM concentration.

These results shown in Fig. 2 illustrate the influence of both contaminant dosage and dynamic equilibrium. The curves show an early regime where the contaminant dosage and accumulation in the cell govern the voltage impacts, which can be brief, on the order of minutes for the 500 μM concentration experiments, or long, taking many hours for the 5 μM concentration such that a steady state was not reached in these experiments. This is followed by a steady state voltage when the cell reaches a dynamic equilibrium, with a balance

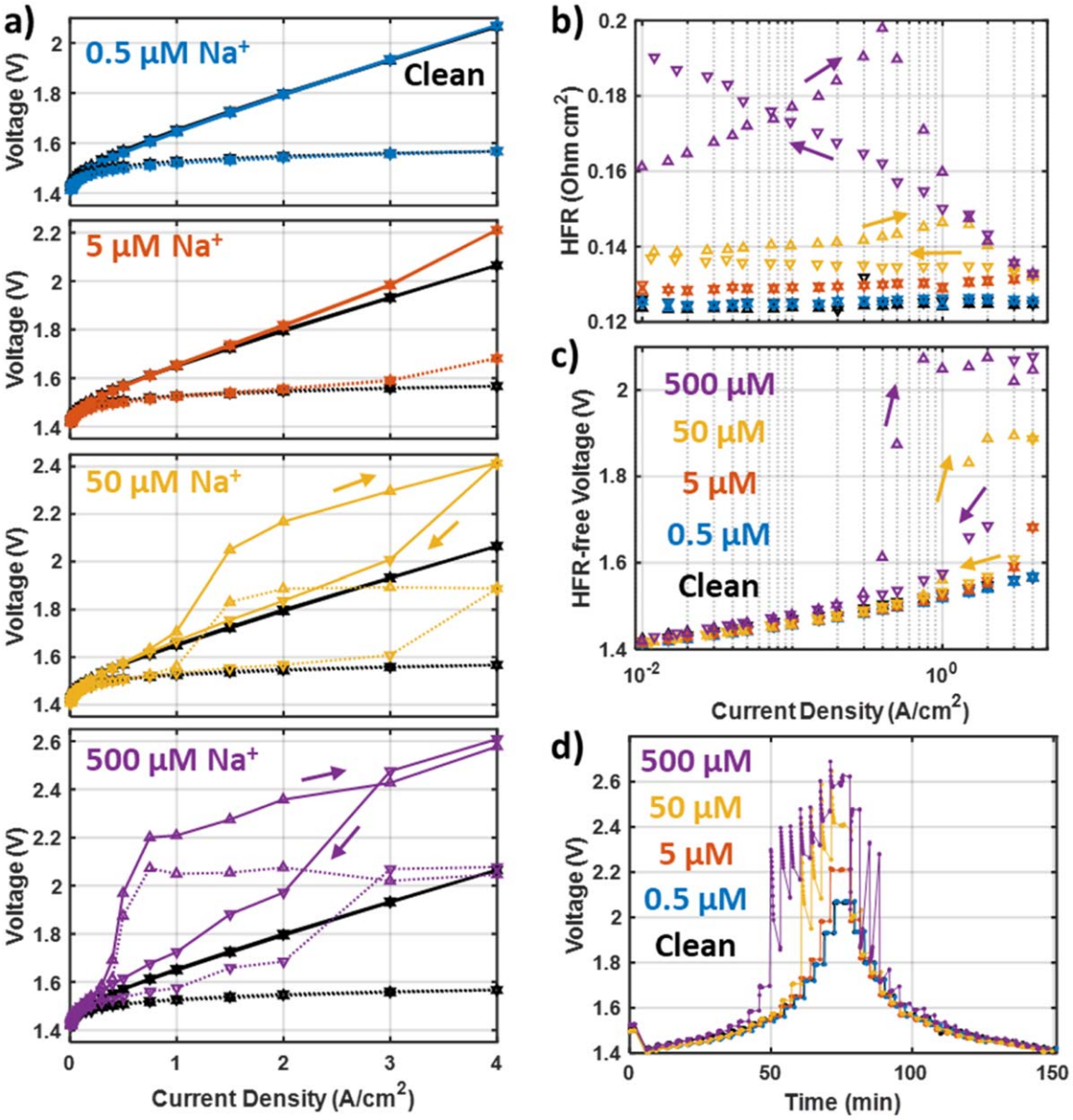

Figure 4. Summary of impacts of NaCl contaminant on polarization curves at different concentrations. (a) Polarization curves (solid) and HFR-free voltage (dotted) for different cation concentrations from 0.5 μM to 500 μM in comparison to performance with clean DI water. All polarization curves are plotted with the same voltage scaling to facili. Points are marked for the ascending and desending polarization curve sweeps with upward and downward facing triangles, respectively, with arrows also indicating the direction of current sweep. The same color and marker scheme is followed throughout. (b) HFR and (c) Tafel plots for the same polarization curves. (d) Cell voltage over time during polarization curve acquisition, showing voltage transients as the current density is stepped.

between ion uptake and escape, which also depends on the contaminant cation and concentration. Both the final steady-state voltage and the time to reach it are notably different depending on the cation and the concentration, particularly with high concentrations and higher valence resulting in larger, faster voltage increases. These effects are governed by a number of complex processes dictating the uptake and escape of ions and their distribution within the cell.

Figure 3 shows a more detailed investigation of the voltage response to contaminants using analysis of impedance spectra recorded during the 2 A cm^{-2} current hold. The observations were qualitatively similar for all contaminants investigated, and $CaCl_2$ was selected as a representative example for Fig. 3 because the greater and more rapid voltage impacts allowed for a clearer illustration of the onset of impedance effects. Figure 3a shows the voltage change over time, with impedance spectra shown in Fig. 3b selected from the points marked in (a) by correspondingly colored stars. Figure 3c shows the time evolution of the HFR values extracted from impedance spectra, alongside the change in the total voltage and the HFR-associated voltage change J*HFR for current density J. It should be noted that with multiple ions present in the membrane the HFR cannot necessarily be interpreted directly as the total ohmic resistance of the cell, as contaminant ions can contribute to the membrane's AC conductivity without contributing to its DC proton conductivity. However, because of the significantly lower conductivity of non-proton cations,[38] an HFR increase does qualitatively indicate accumulation of contaminant cations and an increase in proton resistance.

As described above, only a very small change was observed for the clean cell, including minimal changes to the impedance spectrum, a $\sim$12 mV increase in the total voltage, and a $<$1 mΩ cm^2 decrease in the HFR, which are unrelated to contamination effects. A very similar total voltage change was observed with 0.5 μM Ca^{2+}, although a slightly increasing trend in the HFR after an initial decline is visible, which may indicate the beginning of

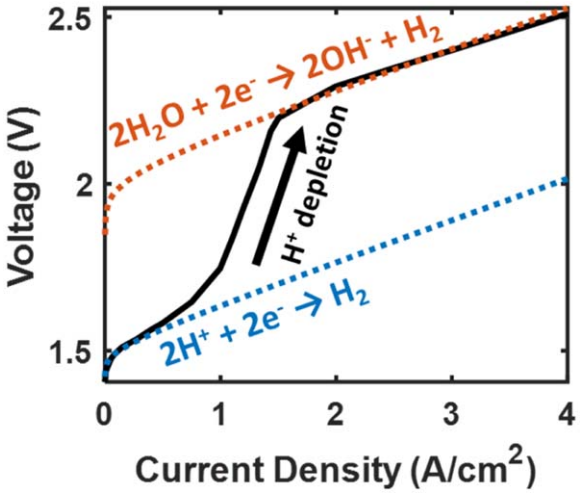

Figure 5. Illustration of the effect of HER mechanism switching caused by cation contaminants on polarization curve shape.

slow Ca^{2+} accumulation in the cell. Significant changes become apparent with 5 μM Ca^{2+}, including an increase of ~6 mΩ cm^2 in the HFR, a ~40 mV increase in the total voltage, and an additional feature appearing in the low frequency range of the impedance spectrum. While the increase in the HFR is clearly pronounced in this case, the change in J*HFR accounts for only about 1/3 of the total voltage change. This suggests that the catalytic processes in the electrodes are being impacted as well as the membrane proton conductivity, which we will discuss in detail below. For the more severe case of 50 μM Ca^{2+}, the total voltage increased by more than 400 mV, with an HFR increases of ~13 mΩ cm^2. The relative proportion of the voltage change from J*HFR is smaller in comparison to the milder 5 μM Ca^{2+} case, with the J*HFR accounting for only ~6% of the total. For 50 and 500 μM Ca^{2+}, the additional impedance feature has grown dramatically larger than the impedance for a clean cell, dominating the overall spectrum. The growth of the low frequency feature results in a much larger overall low frequency impedance, around 1 Ω cm^2 or greater, for 50 and 500 μM Ca^{2+}, in comparison to the ~135 mΩ cm^2 low frequency impedance observed for the clean cell, which includes the normal ohmic resistances and kinetic impedance.

The impedance spectra measured during polarization curves are illustrated in Fig. S4. Figure S5 shows a comparison of the impedance data presented in Fig. 3 to the impedance recorded during polarization curves for the Ca-contaminated cell.

Figure 4 shows the impact from contaminated feed water on polarization curves recorded after the 2 A cm^{-2} hold, with polarization curves and HFR-free voltage shown in (a), HFR in (b), Tafel plots in (c), and polarization curve voltage over time in (d). All the contaminants examined here resulted in qualitatively similar impacts on the polarization curves, and so NaCl was selected as a representative example as the NaCl results best illustrate the different behaviors at low and high contaminant concentrations. Figures S1 and S2 show polarization curves recorded with KCl and $CaCl_2$ contaminants. The trends in the magnitude of voltage impact are similar to those shown in Fig. 2. No significant impact is visible for 0.5 μM contaminants in the feed water, while 5 μM results in moderate impact (~150 mV at 4 A cm^{-2}), and 50–500 μM result in severe impacts (~350–500 mV at 4 A cm^{-2}). KCl contamination (Fig. S1) generally results in similar performance impacts to NaCl, while $CaCl_2$ contamination (Fig. S2) leads to more severe impacts.

Figure 4a shows that the performance impacts from cation contaminants result in distinctively shaped polarization curves. For relatively mild contamination, (5 μM Na^+,) the voltage increase appears as upward curvature at high current densities, primarily impacting the HFR-free voltage, which could be mistaken for mass transport effects impacting the anode. For more severe contamination, (50–500 μM Na^+,) a more unique "S" shape appears in the ascending sweep of the polarization curve. Furthermore, the descending sweep shows significantly lower voltages at moderate to high current densities, resulting in an apparent hysteresis loop in the polarization curves. In all cases there is minimal impact on the voltage at low current densities.

Figure 4b shows that the HFR increases significantly with the concentration of contaminants, which is expected based on lower mobility of contaminant cations[38] and indicates indirectly a loss in proton conductivity from cation displacement. For 5 μM Na^+ the increase in HFR is generally uniform across all current densities, but for 50–500 μM Na^+ the HFR shows significant dependence on the current density. However, the majority of the voltage increase is present in the HFR-free voltage, as shown in Figs. 4a and 4c. This is consistent with prior work on cation contamination in PEM fuel cells,[28,30,31] which showed that kinetic and thermodynamic effects in the cathode were more significant than ohmic impacts on the cell voltage, as well as reference electrode measurements by Zhang et al.[18,19]

The difference between the upward and downward sweeps of the polarization curve is related to voltage transients (shown in Fig. 4d) observed at current densities above the "S bend," where stepping the current density up causes the voltage to rapidly spike upward, and then decay back down. A similar effect also occurs when the current is stepped down, with the voltage rapidly declining, and then gradually returning to higher values. These transient effects cause the polarization curves to be sensitive to the specific time at which the current or voltage is sampled, as shown in Fig. S3, with times shortly after the current step resulting in a more severe "S" shape and wider hysteresis loop. However, the impacts of contaminants are qualitatively similar across a range of times commonly used for polarization curve measurement. These effects appear to be related to both ion redistribution within the cell and ion removal from the cell, as will be discussed in detail below.

Mechanisms of performance impacts.—The results shown above are consistent with previous reports of the performance impacts of cation contaminants on PEMWE.[4,18–24] Contaminant cations increase the proton resistance of the membrane, although this is a relatively small contributor to the overall voltage increase in severely contaminated cells. More significantly, the electric field in the membrane pushes all cations towards the cathode, but because only protons are removed through hydrogen evolution, a concentration polarization in contaminant cations forms across the cell (as illustrated in Greszler et al.,[31] for instance). This results in a depletion of protons in the cathode, leading to thermodynamic and kinetic losses at high current densities. We observed minimal impact on the cell performance at low current density, implying that catalyst poisoning by adsorption is not a significant factor.

However, for PEMWE cells, cathode proton concentration losses do not result in a limiting current behavior, as would be expected from analogy to PEM fuel cells.[27–29] Instead, at high current density the voltage impact plateaus, resulting in the characteristic "S-shaped" polarization curves shown above. This can be explained by a key difference in the available electrode reactions for PEMWE and PEMFCs. For PEMWE, the cathode typically has acidic conditions, and therefore performs the acidic form of the HER, $2H^+ + 2e^- \rightarrow H_2$, $E_0 = 0\ V_{SHE}$, which can also be described as proton reduction. However, the alkaline form of the HER, or water reduction, $2H_2O + 2e^- \rightarrow 2OH^- + H_2$, $E_0 = -0.83\ V_{SHE}$, is also available as a backup reaction that does not require protons as a reactant. A switch in HER mechanism caused by contaminant cations was proposed by Zhang et al.,[18,19] who showed that the cathode outlet water pH increased after operating with sodium-contaminated water on the anode side, indicating that sodium hydroxide had been generated at the cathode.

Such a switch in the HER mechanism can explain the S-shape of polarization curves in the presence of contaminant cations, as

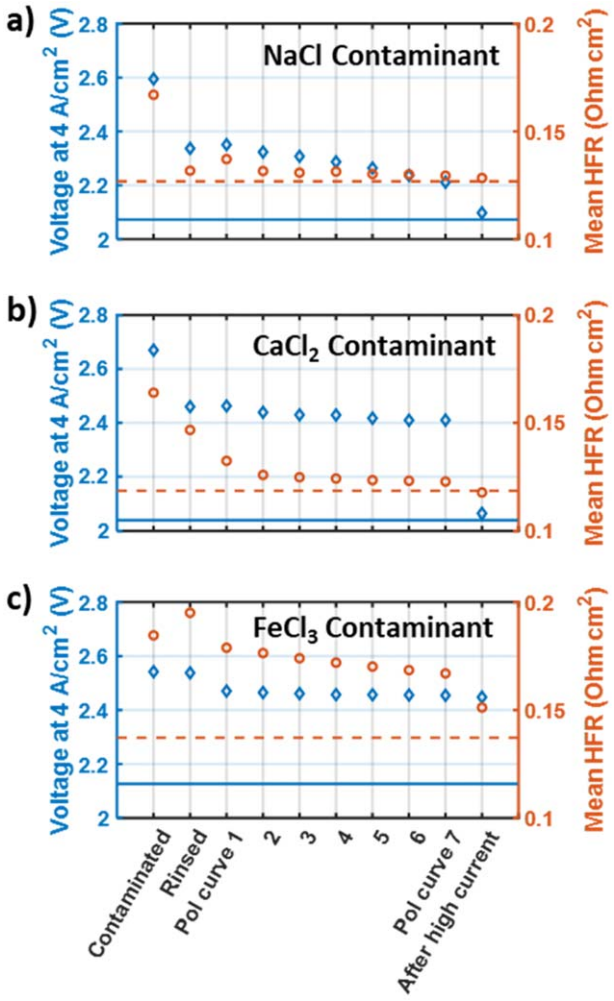

Figure 6. Summary of performance recovery observed during the different recovery protocols, including the cell voltage at 4 A cm^{-2} (blue diamonds, left axis) and the HFR, averaged across all points in the polarization curve (orange, right axis). The baseline performance metrics measured for each cell before contamination are indicated by the horizontal lines on the plot.

illustrated in Fig. 5. Three distinct regimes appear in the S-shaped polarization curve. At low current density, contaminant cations are relatively diffuse in the cell, leaving a relative abundance of protons in the cathode to support proton reduction. There is minimal impact on the cell performance beyond an increased ohmic resistance in the membrane. At moderate current density, the electric field (potential gradient) in the membrane drives contaminant cations to concentrate in the cathode, depleting protons, increasing pH, and leading to a cell voltage increase as the cathode experiences a Nernstian potential shift. At high current density, the cathode proton depletion is sufficient to cause a switch in the HER mechanism from proton reduction to water reduction. This halts the trend toward limiting current from proton starvation of the cathode.

Fundamental investigations have shown that the HER mechanistic switch from proton reduction to water reduction is expected around pH 4 or 5.[39–42] When this occurs, the cell voltage will be increased by both a Nernstian shift in the reversible potential for hydrogen evolution and the slower kinetics of the HER in neutral-alkaline conditions.[39] The Nernstian shift of the reversible cathode potential $E_{0,C}$ is given by:

$$E_{0,C} = -\frac{RT}{F}\ln(a_{H^+}) = \frac{RT\ln(10)}{F}\text{pH}, \quad [1]$$

For gas constant R, temperature T, Faraday constant F, and proton activity a_{H^+}. At 80 C, the pH-potential relationship is $\ln(10)RT/F \approx 70$ mV. In the experimental results presented above, the "flattening" of the HFR-free voltage curve is observed after about 300 mV of HFR-free voltage increase, corresponding to the expected Nernstian potential impact from a pH increase of ~4. This polarization curve feature is therefore consistent with the potential that is expected to drive a change in the HER mechanism.

Given the chloride salts used as contaminants in this study, it is possible that some degree of chlorine evolution occurs during these experiments.[4,24] However, if all the chloride in 500 μM NaCl-contaminated inlet water were consumed, chlorine evolution would contribute a maximum of 8 mA cm^{-2} to the total current. However, in reality some NaCl will exit the anode outlet without any interaction with the cell, and some may participate in an ion exchange, acidifying the outlet water, consistent with the findings of Zhang et al.[18,19] It is also possible that chloride poisoning of the catalysts could impact the cell performance. However, there is minimal impact visible at low currents in Tafel plots (Figs. 4b, S1b, S2b) for contaminated cells, indicating that any kinetic impacts of catalyst poisoning by chloride adsorption are minor in comparison to kinetic effects. Furthermore, chloride adsorption was not clearly evident in cyclic voltammograms recorded with contaminated feed water (Fig. S6). Therefore, we do not believe this to be a significant effect on our performance curves.

The switch in HER mechanism has an important consequence beyond determining the cells current/voltage relationship. The water reduction mechanism produces hydroxides, which can leave the cell paired with contaminant cations. This effect is necessary to explain the alkalinization of the cathode outlet water observed by Zhang et al.[18,19] This creates an electrochemical mechanism for cation removal from PEMWE cells, which does not exist for PEM fuel cells. We expect that cation removal also explains the voltage hysteresis and transient effects described in the previous section. Specifically, significantly lower voltages are measured on the downward sweep of the polarization curve (Fig. 4a), reflection ion removal that occurs at high currents. The transient voltage spikes shown in Fig. 4d reflect rapid redistribution of ions within the cell, followed by a slower re-equilibration process from ion removal and uptake. Importantly, this mechanism can be actively used for cation removal to recover contaminated cells, which we will explore in the following section.

Cell recovery from cation contaminants.—Hydroxide generation on the cathode from water reduction, as discussed above, has important implications for the recoverability of cation contaminants. Hydroxides produced on the cathode can pair with contaminant cations, giving them a counter ion to dissociate from the sulfonic acid groups of Nafion™ ionomer and leave the cell. As this occurs, protons generated on the anode from the OER replace contaminant cations after migrating to the cathode, restoring the Nafion™ to proton form. The observation by Zhang et al.[18,19] that the pH of the cathode outlet water increases when sodium ions are introduced at the anode inlet gives clear corroborating evidence for cation removal by hydroxide generation.

The results of the previous section demonstrate that mechanism switching of the HER depends on current density. Extreme proton depletion in the cathode occurs only with a high electric field in the membrane accompanying high current density. This provides the cell operator the ability to trigger a "cleaning" mechanism at high current. This section will investigate how this phenomenon can be leveraged for contaminant removal and performance recovery.

Several publications have demonstrated removal of contaminant cations through an acid washing of the cell, typically using sulfuric acid,[12,13,20,24] and in one case using carbonic acid from dissolved CO_2.[21] For these acid-wash methods, a sufficient excess of protons must be provided to remove most contaminant cations once

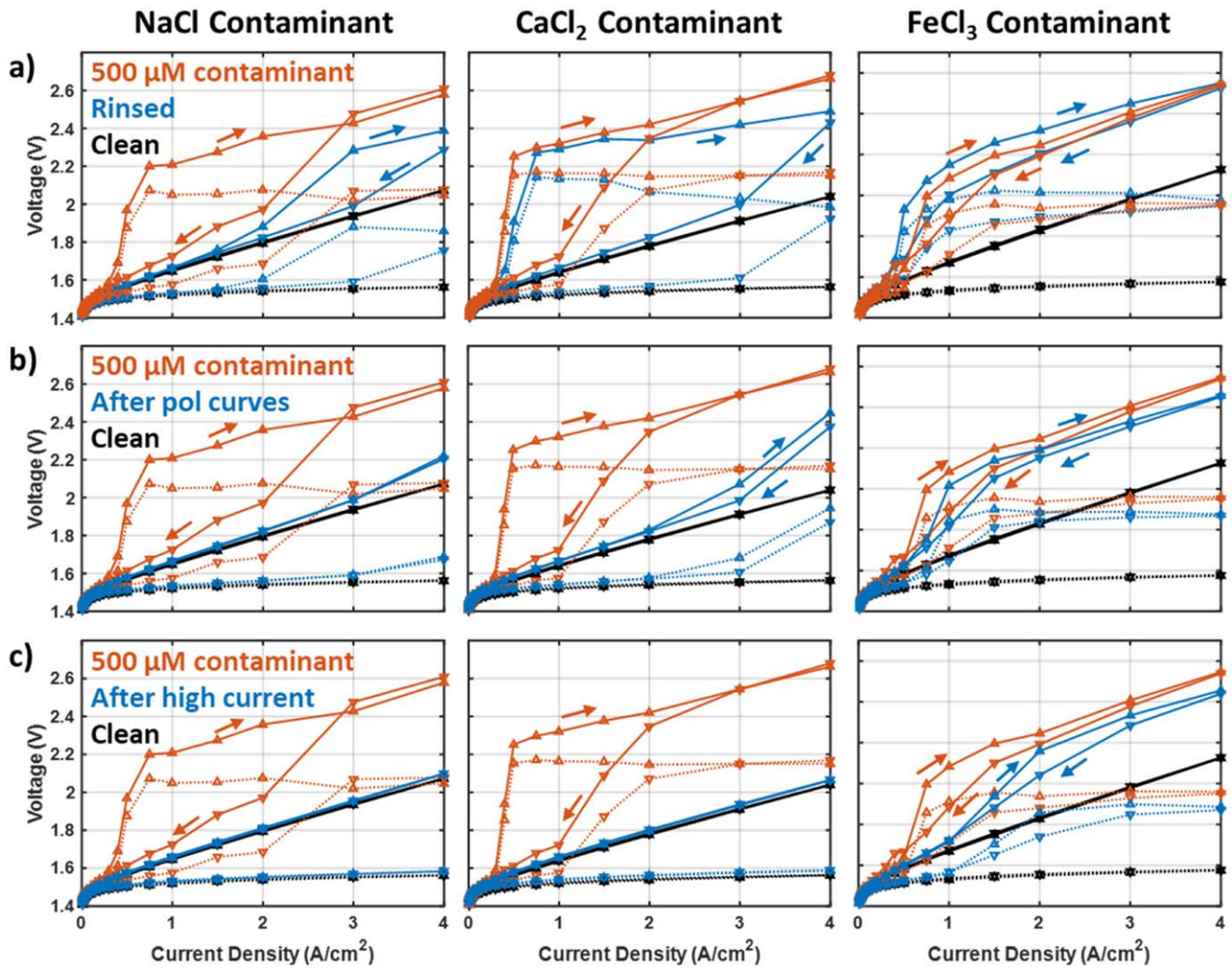

Figure 7. Comparison of polarization curves (solid lines) and HFR-free voltage (dotted lines) for different contaminants after different recovery procedures (blue) in comparison to measurements with contaminated water feed (orange) and baseline cell performance in clean water (black). (a) Performance in a single polarization curve recored after clean deionized water was flowed over the cell overnight. (b) Performance on the seventh polarization curve recorded in clean deionized water. (c) Performance after a high current density recovery protocol conducted with clean water. Arrows indicate the direction of current sweep.

equilibrium is reached between the membrane and the acid solution. In contrast, the mechanism demonstrated here generates the needed protons in situ. Previous publications have also demonstrated partial recovery from restoring a clean deionized water feed to the cell, which may be to some extent to re-equilibration of the cell with deionized water or to the current-driven mechanism discussed here.

The experiments presented in this section will compare performance recovery after: (1) restoring a clean deionized water feed, (2) repeating a polarization curve measurement with a clean water feed, and (3) applying a high current density to deliberately drive water reduction and hydroxide generation. The results of these experiments are shown in Figs. 6 and 7, comparing Na^+, Ca^{2+}, and Fe^{3+}, in all cases introduced at a concentration of 500 μM during a 2 A cm^{-2} current hold until a steady-state voltage was reached. Fe^{3+}, which is representative of transition metal contaminants that may leach from system components, was included for this investigation as a potentially difficult to remove trivalent cation with more complex solubility behavior in comparison to Na^+ and Ca^{2+}. Removal of iron and other transition metal contaminants is further of interest because these ions can catalyze Fenton reactions and accelerate membrane chemical degradation.[11]

Figure 6 summarizes the results of these experiments by showing the voltage at 4 A cm^{-2} and the mean HFR values for the different recovery procedures. Corresponding polarization curves are shown in Fig. 7, including baseline and contaminated polarization curves for comparison.

In the first case, labeled "Rinsed" in Figs. 6 and 7a, the cell performance was measured after resting overnight with clean deionized water flowing over the anode and cathode. Additional analysis, including Tafel plots and HFR as a function of current density, is shown in Fig. S7. For Na^+, the water rinse appears to result in a significant recovery of the performance, although contaminant effects are clearly still present in the cell, leading to 300–400 mV of excess losses at 4 A cm^{-2}. Relatively minor recovery is visible for the Ca^{2+} contaminant, while the Fe^{3+} contaminant shows no recovery from the water rinse. This trend with the contaminant is expected following the affinity of each cation for Nafion™.

Both the return to a clean water feed and the operation of the cell may have contributed to the observed recovery. To investigate the recovery induced by cell operation in the standard current density window, the cell was re-contaminated with a 500 μM solution and then seven consecutive polarization curves were recorded over approximately 18 h with clean feed water. This procedure was done without an overnight rinse, but took a similar overall time to the rinse procedure. The voltage and HFR for all the sequential polarization curves are summarized in Fig. 6, while the final polarization curve from this sequence is plotted in Fig. 7b.

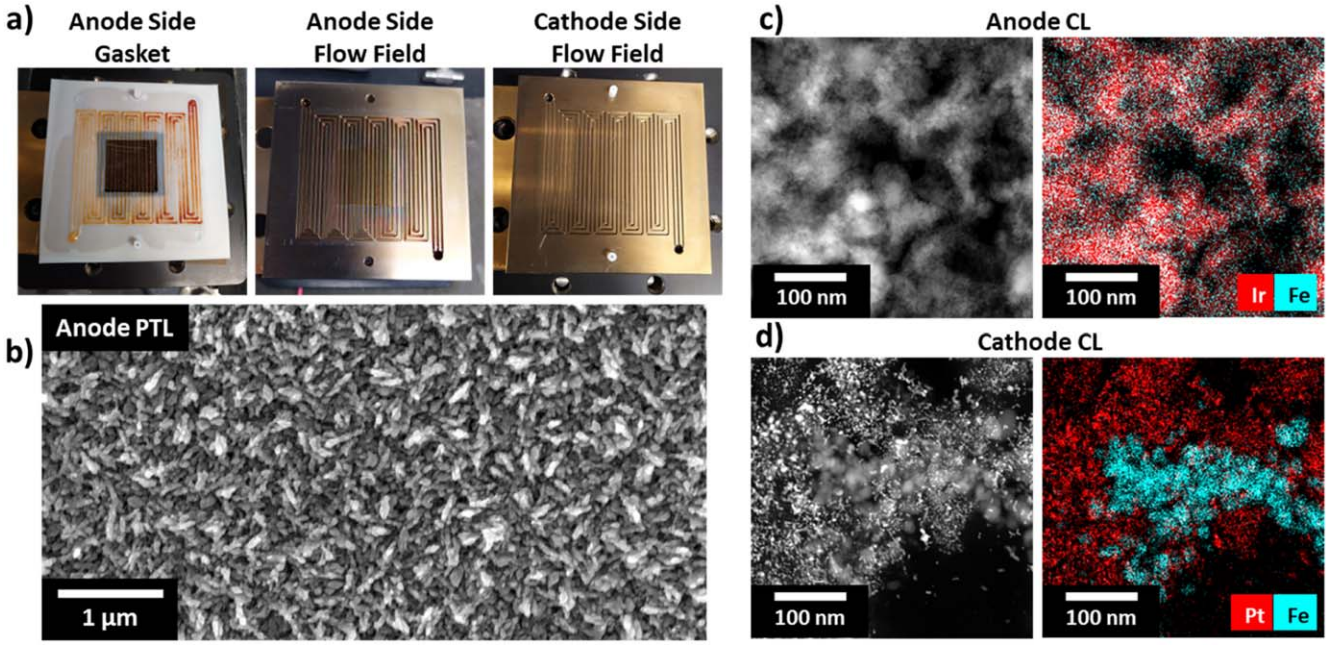

Figure 8. Images showing solid iron deposits in the the cell after contamination with $FeCl_3$ and the recovery protocol. (a) Photographs of the inside of the disassembled cell hardware, showing residual Fe solids on the anode-side gasket, PTL, and flow field, but no visible deposits on the cathode side flow field. (b) Scanning electron microscope image (secondary electron detector) showing crystallites of iron oxide deposited on the anode PTL facing toward the flow field, at a region aligned to the flow channel. (c)–(d) STEM-EDS maps showing Fe deposits in the anode catalyst layer (c) and cathode catalyst layer (d). Annular dark field STEM images are shown at left, with corresponding elemental maps at the right showing Ir and Pt in red and Fe in cyan.

Additional analysis shown in Fig. S8. In all cases, repeated polarization measurement resulted in much more significant performance recovery than rinsing with deionized water alone. The same trend in the degree of recovery by contaminant was observed, with most of the impact from Na^+ contaminants being recovered and only minor recovery from Fe^{3+} contaminants. This result provides evidence that cation contaminant removal can occur from a current-driven process. However, the recovery observed from repeated polarization curves is incomplete, and Fig. 6 shows the progress of cell recovery is slowing as more polarization curves were recorded, without clearly trending toward full recovery, especially for Ca^{2+} and Fe^{3+}.

A final procedure was tested to investigate the effect of deliberately applying a very high current density to drive contaminant removal through hydroxide production on the cathode. This procedure, illustrated in Fig. S9, applied 4 A cm^{-2}, 6 A cm^{-2} and 8 A cm^{-2} to the cell sequentially for one hour each, with polarization curves and holds at 2 A cm^{-2} in between to benchmark the cell performance. This was conducted after the repeated polarization curve test without re-contamination of the cell. The results recorded after this protocol are shown in Figs. 6 and 7c, labeled "After high current," with additional analysis in Fig. S9. These measurements demonstrate almost complete recovery of the initial cell performance for Na^+ and Ca^{2+}, with the HFR recovering within 1 mΩ cm^2 of the initial value and the cell voltage recovering within 25 mV of the initial value at 4 A cm^{-2}. The recovery for Fe^{3+} was more modest, although still improved in comparison to the other recovery protocols tested.

These results demonstrate that a current-driven recovery process can be highly effective for some contaminants such as Na^+ and Ca^{2+}, delivering near complete recovery of the initial performance even for highly contaminated cells. The much poorer recovery for Fe^{3+} may be in part related to its high valence state and affinity for Nafion™, although the solubility of Fe cations may also present a challenge, as explored in the next section. However, the high current density and voltage applied to the cell during a high-current recovery procedure of this type will also lead to significant generation of heat, which will likely limit its practical application to electrolyzer stacks.

Characterization of iron deposits in PEMWE cell after $FeCl_3$ contamination.—Transition metal contaminants, such as iron, have more complex behavior than tap water cations, creating the possibility to form solid deposits in the cell. It has been previously reported that some transition metal contaminants in PEMWE cells can deposit on the cathode catalyst surface, leading to poisoning of the catalyst.[23]

The iron contamination test reported in the previous section left deposits on the anode side gasket and PTL that were visible upon disassembly, as shown in Fig. 8a. These deposits were most visible on the gasket at the locations of the flow channels and ranged in color from dark red near the inlet to pale yellow near the outlet. They were visible on the PTL as dark stripes at the channel locations, as well as discoloration of the flow field channels. There were no visible deposits on the cathode side. Iron deposition on the anode is expected from Pourbaix diagrams,[43–46] which indicate that Fe_2O_3 (red iron oxide) is stable in the near-neutral pH and oxidizing conditions present in the anode flow channels. The color change from the cell inlet to outlet may be due to formation of $FeO(OH)\cdot H_2O$ (yellow iron oxide) or another phase, possibly from the increased presence of crossover hydrogen near the cell outlet, or from a decreased concentration of oxide deposits resulting in a paler color. Scanning electron microscopy (SEM) was used to examine the dark stripes on the PTL facing the flow channels and showed submicron crystallites had formed on the PTL surface (Fig. 8b).

The CCM was further cross-sectioned and examined by scanning transmission electron microscopy (STEM) and energy dispersive X-ray spectroscopy (EDS) to identify contaminant deposits inside the CCM (Figs. 8c, 8d). Iron-containing deposits were present throughout the anode catalyst layer and are expected to form by a similar process to the deposits observed on the PTL. Iron-containing deposits were also found in the cathode catalyst layer, although in more localized clusters rather than distributed throughout. Pourbaix diagrams[43–46] show that FeO or Fe_3O_4 is stable at low potentials and moderately alkaline conditions. The observation of iron oxide deposits in the cathode therefore supports the conclusion that the cathode pH increases as a result of cation contamination. Furthermore, the formation of solid iron oxide deposits and the

poor solubility of iron cations in neutral to alkaline conditions may hinder the removal of iron from the cell as a soluble hydroxide. This may in part account for the relatively poor recovery from Fe contamination reported in the previous section. It is also notable that these deposits persist in post-mortem analysis, however, as when current is removed from the cell the pH in the ionomer is expected to fall to the point where Fe^{2+} or Fe^{3+} cations would again be soluble. The relatively localized solid iron oxide deposits may therefore be formed in voids of the cathode catalyst layer, where a lack of ionomer may prevent dissolution.

These observations suggest some obstacles to recovering the performance impacts of transition metal contaminants, such as iron, by the high-current process that was effective for sodium and calcium. First, solid Fe-containing deposits in the cell may provide a reservoir of contaminants that can be introduced into the membrane and ionomer over time. Second, the insolubility of Fe cations at high pH, which leads to formation of solid iron deposits on the cathode, may inhibit cation removal by hydroxide generation on the cathode.

Conclusions

This investigation examined the impact of cation contaminants on PEMWE cell performance and the recovery of contaminated cells through a current-driven process. We tested the performance impacts of feed water containing representative tap water cations at concentrations ranging from 0.5–500 μM, with conductivities spanning from ASTM Type II to tap-water levels. We found clear short-term performance impacts for concentrations of 5 μM and greater, including solutions that would be classified as ASTM Type II (>1 MΩ cm). This demonstrates that use of ASTM Type II water risks introducing significant performance impacts for PEMWE, depending on the ions present. Significant impacts may occur from even lower ion concentrations over a longer timeframe, potentially impacting durability measurements. Higher contaminant concentrations (50–500 μM) led to large cell voltage increases (300–600 mV) that reached a stable plateau within minutes to hours, depending on the concentration. Instead of reaching a limiting current behavior, the increased voltage from high contaminant concentrations plateaus in "S-shape" polarization curves. We conclude that this results from a change in the HER mechanism from proton reduction to water reduction, driven by proton depletion in the cathode, as postulated by prior studies.

These results identify several signatures of cation contamination in PEMWE cells, which are useful for practical diagnosis of contaminant effects. These signatures include:

- *Polarization curve shape:* For relatively mild contamination, additional losses appear with an onset at high current densities and an upward curvature, superficially resembling mass-transport-induced losses. For relatively severe contamination, the high-current-density losses level off as a result of the HER mechanism change, creating an "S-shaped" pol curve.
- *Hysteresis in the polarization curve:* The high-current-density region of the polarization curve is asymmetric with the direction of the polarization curve sweep. The descending sweep shows lower voltage than the ascending sweep, most likely as a result of ion removal at high currents, creating a hysteresis loop when plotted together. Recording and examining both sweeps of the polarization curve is therefore a good practice for identifying potential effects from cation contaminants.
- *Transient voltage spikes:* For significantly contaminated cells, when the current is stepped up during a current-staircase polarization curve, the voltage spikes up and then decays down over a period of 10's of seconds. A similar reversed feature appears as the current is stepped down.
- *Impedance changes:* Contaminated cells show an increase in HFR as well as an additional impedance feature observed at low frequencies, presumably related to proton depletion in the cathode.

We further demonstrated that contaminants can be removed from the cell, especially by the application of high current density, which triggers the water reduction mechanism to produce hydroxide as counter ions that remove contaminant cations. A protocol including a 1 hr hold at 8 A cm^{-2} achieved near-complete recovery of cells contaminated with Na and Ca. This protocol was less effective at recovering from Fe contaminants, which may be related to the insolubility of Fe under high pH conditions and solid Fe-containing deposits observed with microscopy. The results support the key conclusion that contaminant cations can be removed from PEMWE cells without the use of an acid. The oxygen evolution reaction instead can serve as a proton source to replace contaminant cations removed by water reduction on the cathode.

Together, the results presented here can improve understanding of cation impacts in PEMWE, inform development of strategies to mitigate or recover performance losses, as well as improve the consistency and rigor of electrolysis research.

Acknowledgments

This work was authored by the National Renewable Energy Laboratory, operated by Alliance for Sustainable Energy, LLC, for the U.S. Department of Energy (DOE) under Contract No. DE-AC36–08GO28308. This work was conducted as part of the Hydrogen from Next-generation Electrolyzers of Water (H2NEW) consortium, funded by the U.S. DOE Office of Energy Efficiency and Renewable Energy (EERE) Hydrogen and Fuel Cell Technologies Office (HFTO). Electron microscopy research was supported by the Center for Nanophase Materials Sciences (CNMS), which is a U.S. Department of Energy, Office of Science User Facility at Oak Ridge National Laboratory. The views expressed in the article do not necessarily represent the views of the DOE or the U.S. Government. The U.S. Government retains and the publisher, by accepting the article for publication, acknowledges that the U.S. Government retains a nonexclusive, paid-up, irrevocable, worldwide license to publish or reproduce the published form of this work, or allow others to do so, for U.S. Government purposes. The authors thank Danielle Henckel, Chaiwat Engtrakul, Huyen Dinh, Sarah Blair, and Megan Holtz for useful conversations.

ORCID

Elliot Padgett https://orcid.org/0000-0001-9034-2335
Haoran Yu https://orcid.org/0000-0001-7304-2840
Jacob Wrubel https://orcid.org/0000-0002-3347-0768
Guido Bender https://orcid.org/0000-0003-3777-4707
Bryan Pivovar https://orcid.org/0000-0001-5181-5363
Shaun M. Alia https://orcid.org/0000-0002-7647-9383

References

1. B. Pivovar, N. Rustagi, and S. Satyapal, *Electrochem. Soc. Interface*, **27**, 47 (2018).
2. K. Ayers et al., *Annu. Rev. Chem. Biomol. Eng.*, **10**, 219 (2019).
3. B. S. Pivovar, M. F. Ruth, D. J. Myers, and H. N. Dinh, *Electrochem. Soc. Interface*, **30**, 61 (2021).
4. H. Becker et al., "Impact of impurities on water electrolysis: a review." *Sustainable Energy Fuels*, **7**, 1565 (2023), https://pubs.rsc.org/en/content/articlelanding/2023/se/d2se01517j.
5. E. Taibi, H. Blanco, R. Miranda, and M. Carmo, *Green Hydrogen Cost Reduction: Scaling up Electrolysers to Meet the 1.5^{0}C Climate Goal*, International Renewable Energy Agency (2020), https://irena.org/publications/2020/Dec/Green-hydrogen-cost-reduction ISBN: 978-92-9260-295-6.
6. Nel Hydrogen, (2023), https://nelhydrogen.com/faq/.
7. ASTM D1193: Standard Specification for Reagent WaterASTM, (2024), https://astm.org/d1193-06r18.html.
8. N. Danilovic et al., *ECS Trans.*, **75**, 395 (2016).
9. C. Capuano, *Manufacturing Challenges, Opportunities, and Successes for PEM Electrolysis at Scale*, *3rd International Conference on Electrolysis, Golden Colorado* (2022).
10. K. Ayers, *Low Temperature PEM Cells Leveraging Hydrogen and Oxygen Evolution Electrodes*, *242nd ECS Meeting, Atlanta Georgia* (2022).
11. S. H. Frensch et al., *J. Power Sources*, **420**, 54 (2019).
12. S. Sun, Z. Shao, H. Yu, G. Li, and B. Yi, *J. Power Sources*, **267**, 515 (2014).
13. G. Wei et al., *Int. J. Hydrogen Energy*, **35**, 3951 (2010).
14. G. Bender et al., *Int. J. Hydrogen Energy*, **44**, 9174 (2019).

15. D. Myers, *H2NEW Hydrogen (H2) from Next-generation Electrolyzers of Water: H2NEW LTE: Task 2 Benchmarking and Performance*, *DOE Hydrogen Program 2023 Annual Merit Review* (2023), https://hydrogen.energy.gov/docs/hydrogenprogramlibraries/pdfs/review23/p196b_myers_2023_p-pdf.pdf.
16. M. A. Khan et al., *Energy Environ. Sci.*, **14**, 4831 (2021).
17. A. T. Mayyas, M. F. Ruth, B. S. Pivovar, G. Bender, and K. B. Wipke, *Manufacturing Cost Analysis for Proton Exchange Membrane Water Electrolyzers NREL/TP-6A20-727401557965*, National Renewable Energy Laboratory (2019), http://osti.gov/servlets/purl/1557965/.
18. L. Zhang, X. Jie, Z.-G. Shao, X. Wang, and B. Yi, *J. Power Sources*, **241**, 341 (2013).
19. L. Zhang et al., *Int. J. Hydrogen Energy*, **37**, 1321 (2012).
20. X. Wang et al., *Electrochim. Acta*, **158**, 253 (2015).
21. U. Babic, M. Zlobinski, T. J. Schmidt, P. Boillat, and L. Gubler, *J. Electrochem. Soc.*, **166**, F610 (2019).
22. M. Zlobinski et al., *J. Electrochem. Soc.*, **167**, 144509 (2020).
23. F. Andolfatto, R. Durand, A. Michas, P. Millet, and P. Stevens, *Int. J. Hydrogen Energy*, **19**, 421 (1994).
24. M. Schalenbach et al., *J. Electrochem. Soc.*, **169**, 094510 (2022).
25. N. Li, S. S. Araya, X. Cui, and S. K. Kær, *J. Power Sources*, **473**, 228617 (2020).
26. C. Rakousky et al., *J. Power Sources*, **326**, 120 (2016).
27. T. Okada, *Handbook of Fuel Cells* (Wiley, Ltd, Hoboken, New Jersey, U.S.) (2010).
28. A. Z. Weber and C. Delacourt, *Fuel Cells*, **8**, 459 (2008).
29. M. Sulek, J. Adams, S. Kaberline, M. Ricketts, and J. R. Waldecker, *J. Power Sources*, **196**, 8967 (2011).
30. B. Kienitz, B. Pivovar, T. Zawodzinski, and F. H. Garzon, *J. Electrochem. Soc.*, **158**, B1175 (2011).
31. T. A. Greszler, T. E. Moylan, and H. A. Gasteiger, *Handbook of Fuel Cells* (Wiley, Ltd, Hoboken, New Jersey, U.S.) (2010).
32. G. Bender, M. Angelo, K. Bethune, and R. Rocheleau, *J. Power Sources*, **228**, 159 (2013).
33. W. M. Haynes and P. Vanysek, "Ionic conductivity and diffusion at infinite dilution." (2012) *CRC Handbook of Chemistry and Physics* 93rd Edition ed.(CRC Press, Boca Raton, FL).
34. A. Azoulay, P. Garzon, and M. J. Eisenberg, *J Gen Intern Med*, **16**, 168 (2001).
35. A. Chapotot, G. Pourcelly, and C. Gavach, *J. Membr. Sci.*, **96**, 167 (1994).
36. R. Tandon and P. N. Pintauro, *J. Membr. Sci.*, **136**, 207 (1997).
37. H. L. Yeager, *Perfluorinated Ionomer Membranes, ACS Symposium Series.* (American Chemical Society, Washington, DC) **180**, 41 (1982).
38. I. A. Stenina, P. Sistat, A. I. Rebrov, G. Pourcelly, and A. B. Yaroslavtsev, *Desalination*, **170**, 49 (2004).
39. T. Shinagawa, A. T. Garcia-Esparza, and K. Takanabe, *ChemElectroChem*, **1**, 1497 (2014).
40. B. E. Conway and B. V. Tilak, *Electrochim. Acta*, **47**, 3571 (2002).
41. J. B. Mitchell, M. Shen, L. Twight, and S. W. Boettcher, *Chem Catalysis*, **2**, 236 (2022).
42. Z. Zhou et al., *Energy Environ. Sci.*, **13**, 3185 (2020).
43. A. Jain et al., *APL Mater.*, **1**, 011002 (2013).
44. A. M. Patel, J. K. Nørskov, K. A. Persson, and J. H. Montoya, *Phys. Chem. Chem. Phys.*, **21**, 25323 (2019).
45. K. A. Persson, B. Waldwick, P. Lazic, and G. Ceder, *Phys. Rev. B*, **85**, 235438 (2012).
46. A. K. Singh et al., *Chem. Mater.*, **29**, 10159 (2017).